



Journal of Engineering Sciences
Assiut University
Faculty of Engineering
Vol. 42
No.5
September 2014
PP. 1193 – 1214



DEVELOPMENT, VERIFICATION AND VALIDATION OF AN IN-HOUSE CFD CODE FOR WEAKLY COMPRESSIBLE FLOW

**Walid J. Al-Nahari^{*}, Mohammed F. F. El-Dosoky,
 Mohammed M. Abdelghany, and Hamdy M. Shafey**

Mechanical Eng. Dept., Faculty of Engineering, Assiut University, Assiut, Egypt

(Received 24 September 2014; Accepted 28 October 2014)

ABSTRACT

The work of this paper represents the first stage of a whole modeling and computational solution procedure for an on-going research on agricultural fires at the laboratory of environmental research, Assiut University. The paper presents an accurate and efficient semi-implicit pressure-based algorithm developed for solving numerically the conservation equations governing weakly compressible single-fluid flows. The algorithm uses a finite-volume technique applied to structured non-orthogonal multi-block curvilinear meshes with co-located grid arrangement. An in-house CFD code has been developed to implement the numerical solution of the present algorithm. The code is an integrated one consisting of the main elements, the pre-processor, the solver and the post-processor. This in-house CFD code undergoes a standard verification and validation process using a variety of standard test cases covering broad range of CFD applications. The results of the present code for all test cases are in good agreement with those of the well-established reference CFD codes. This insures the present code verification and validation.

Keywords: CFD codes; weakly compressible flows; lid-driven square cavity flow; flow over pump in a channel; unsteady flow past downstream facing step; flow over a hot flat plate.

1. Introduction

One of the worldwide problems is the annually frequent occurrence of agricultural fires that are intentionally set by human or naturally developed (by e.g. lightning and hot weather). The term agricultural fire denotes the uncontrolled burning of agricultural solid fuel in an open atmosphere. It can be classified as a free-standing fire that begins and propagates in planted crops, savannah, forests, and agricultural residues. Scientists and researchers for several decades have tried to predict the propagation of agricultural fires, with the goal of limiting its environmental pollution (thermal, gaseous, and particulates), serious health effects, and great economic loss. The propagation of agricultural fires is an extremely complex phenomenon in which all effects found in chemically reacting turbulent flows with Mach number less than 0.3 are linked together. These effects include flow

^{*} Corresponding author.

Email address: walid_yemen@yahoo.com

turbulence parameters, combustion, kinetics, thermal radiation, and multiphase nature of the flow. Consequently, it was a formidable task (for several years) to develop a unified computational model for the propagation of agricultural fires. Recently, this has become possible with the development of CFD approach from the first principles via solution of the basic conservation equations of the flow.

Most of the published fire models based on exciting commercial CFD codes are generally limited to compartment fires [1-4] and free-standing fires [5-7] other than agricultural ones. Available research works on CFD modeling of agricultural fires [8-14] incorporate simplifying assumptions and cannot be extended to the real physical situation. Such real situation may be described by the complex nature and the generality of the unsteady, three dimensional, multiphase flow of the fire products associated with the multi-class agricultural solid fuel. Recently El-Zohri et al. [15] have developed a mathematical model for wind-driven surface agricultural fires. Their model considered a simple configuration of a homogenous solid fuel bed consisting of thermally thin agricultural particles. The fuel bed uniformly covers a horizontal plane surface of a thermally insulated non-porous ground. The model also simply treated the fire of the agricultural fuel particles as stationary solid phase linked with the flow of the gas phase containing fine soot particles. El-Zohri et al. [16] have extended their previously developed model to account for the soot deposition mechanism based on Eulerian-Eulerian approximate approach for the description of the gas-soot particles flow. The predicted results of these two research works were obtained using a special algorithm for the numerical solution of the gas phase flow equations together with a fourth-order Runge-Kutta method for the solution of the stationary solid phase equations.

The limitations, simplifying assumptions, and approximations imposed by the previous works indicate the need for an appropriate algorithm which is capable to solve the flow equations for gas phase with wide conditions of real agricultural fires. The pressure of the gas phase under real fire conditions is almost thermodynamically constant and influences the fluid motion only through its spatial derivatives present in the momentum equations. However, the gas density varies due possible small changes of the gas pressure (around its fixed thermodynamic value) in addition to changes in temperature or gas composition. With such density variations, the resulting gas flow can be regarded as a weakly compressible flow. These real conditions of the gas flow were the motive of the present work as the first stage of the road map of a whole computational solution procedure for agricultural fire modeling.

The aim of the present work is to develop an accurate and efficient semi-implicit pressure-based algorithm with in-house CFD code. This algorithm deals with a new proposed methodology for solving Navier-Stock equations and energy equation that govern weakly compressible single-fluid flows. Turbulent as well as laminar flow conditions are considered. The present algorithm uses a suitable precise finite-volume discretization technique for geometrically complex space domains. This technique employs structured non-orthogonal multi-block boundary-fitted curvilinear meshes with co-located grid arrangement. High order schemes that are used to approximate adjective, diffusive, and non-linear terms, connected with multi-block partitioning techniques, are the main contributions of the present work. The CFD code of the present developed algorithm undergoes a standard verification and validation (V&V) process by applying it to four test cases and comparing its results with those obtained with other well-established reference CFD codes.

2. Development of the numerical algorithm

This section concisely describes in detail the basics and features of the algorithm developed in the present work. The algorithm is a semi-implicit pressure-based one that can be used to numerically solve the conservation equations for weakly compressible flow of a single phase fluid.

2.1 Governing equations

When turbulence is considered in weakly compressible flows Favre-averaged conservation equations are commonly used to describe the time mean (short time averaged) flow values. These equations are also known as Reynolds Averaged Navier-Stokes (RANS) equations. Additional two differential equations are used to account for the turbulent components (temporal fluctuations) of the flow. These two equations are known as turbulence sub-model. The general time dependent three dimensional Favre-averaged conservation equations describing the weakly compressible flow of single-phase fluid, with the standard k - ε sub-model for turbulence can be expressed in the following general form for a conserved transport property [17]:

$$\frac{\partial(\rho\phi)}{\partial t} + \nabla \cdot (\rho \vec{U} \phi) = \nabla \cdot (\Gamma_\phi \nabla \phi) + S_\phi \quad (1)$$

where \vec{U} is the flow velocity vector, and ϕ is the generic form of the transport fluid property having a corresponding diffusive exchange coefficient Γ_ϕ and a source term S_ϕ . Table 1 shows the expressions of the generic form, ϕ , and associated functions, Γ_ϕ and S_ϕ , in Cartesian coordinates for each transport property considered in the conservation equations. A simplified form of Equation (1) for incompressible flow can be obtained with $\rho = \text{constant}$.

Some quantities and terms appearing in Table 1 are explained in order as follows. The specific enthalpy energy, h , of the single fluid flow is defined to be zero at a reference temperature T_{ref} and can be expressed as a function of the flow temperature by:

$$h = \int_{T_{\text{ref}}}^T c_p(T) dT \quad (2)$$

substituting for the known function of the specific heat $c_p(T)$ and performing integration, Equation (2) results in a definite relation between the enthalpy h and the temperature T of the fluid flow. This relation is used to convert the resulting enthalpy field to the temperature field in the numerical solution. The effective turbulent viscosity, μ_e , is the sum of the molecular dynamic viscosity, μ , and turbulent viscosity, μ_t , expressed in terms of the turbulence properties k and ε as:

$$\mu_t = \rho c_\mu \frac{k^2}{\varepsilon} \quad (3)$$

Table 1.

The flux and source term for the conservation equations.

| Transport property | ϕ | Γ_ϕ | S_ϕ |
|--|---------------|------------------------------------|---|
| Mass | 1 | 0 | 0 |
| Momentum | u | μ_e | $-\frac{\partial p}{\partial x} + \frac{\partial}{\partial x} \left(\mu_e \frac{\partial u}{\partial x} \right) + \frac{\partial}{\partial y} \left(\mu_e \frac{\partial v}{\partial x} \right) + \frac{\partial}{\partial z} \left(\mu_e \frac{\partial w}{\partial x} \right) + F_x$ |
| | v | μ_e | $-\frac{\partial p}{\partial y} + \frac{\partial}{\partial x} \left(\mu_e \frac{\partial u}{\partial y} \right) + \frac{\partial}{\partial y} \left(\mu_e \frac{\partial v}{\partial y} \right) + \frac{\partial}{\partial z} \left(\mu_e \frac{\partial w}{\partial y} \right) + F_y$ |
| | w | μ_e | $-\frac{\partial p}{\partial z} + \frac{\partial}{\partial x} \left(\mu_e \frac{\partial u}{\partial z} \right) + \frac{\partial}{\partial y} \left(\mu_e \frac{\partial v}{\partial z} \right) + \frac{\partial}{\partial z} \left(\mu_e \frac{\partial w}{\partial z} \right) + F_z$ |
| kinetic energy of turbulence | k | $\frac{\mu_e}{\sigma_k}$ | $G_k + G_b - \rho \varepsilon$ |
| Dissipation rate of kinetic energy of turbulence | ε | $\frac{\mu_e}{\sigma_\varepsilon}$ | $C_{1\varepsilon} \frac{\varepsilon}{k} (G_k + C_{3\varepsilon} G_b) - C_{2\varepsilon} \rho \frac{\varepsilon^2}{k}$ |
| Enthalpy | h | $\frac{\mu_e}{\sigma_h}$ | \dot{Q} |

The quantities σ_k , σ_ε and σ_h are the Prandtl numbers for k , ε , and h , respectively. The thermodynamic pressure, p , of the gas flow can be expressed in terms of the density ρ and temperature T using the ideal gas equation of state. Expressions for the shear and buoyancy turbulence production/destruction terms G_k and G_b , and the values for the coefficients, $C_{1\varepsilon}$, $C_{2\varepsilon}$, and $C_{3\varepsilon}$, can be found elsewhere [17].

Equation (1) can be used with some mathematical modifications to deal with the special cases of laminar flow or flow field in a geometrically complex space domain bounded by curved surfaces. The equations for the case of laminar flow can be obtained by eliminating the generic properties k and ε with the corresponding reduction of the diffusive exchange coefficients μ_e to its normal value of μ . For the other case the flow equations have to be transformed into general curvilinear coordinates, allowing the grids for numerical solution to conform to the boundaries of the complex space domain. The transformation of the flow equations is achieved using the appropriate known relations between the prescribed curvilinear coordinate system and the corresponding Cartesian coordinate system. The partial differentials in the flow equations can be transformed to the required curvilinear coordinates using the chain rule of the differentials [18].

2.2 Domain discretization

The foundation of the numerical solution is to approximate the continuous fields by values at discrete points in space and time. These values are obtained by solving the linear algebraic difference equations approximating the differential equations of the flow. Therefore discretization of the continuous flow field in time and space should be carried out using suitable time steps for the time domain and a finite volume technique for the

space domain. Working with a geometrically complex space domain this technique begins with partitioning the whole space domain into multi-blocks. The space sub-domain associated with each block is by turn discretized into structured non-orthogonal boundary-fitted curvilinear mesh of cells with finite volumes. Finite volume discretization has the ability to handle near discontinuous flow features. Each cell inside the space sub-domain of the block is termed interior cell over which the conservation equations of the flow, Equation (1), are applied. Associated with the mesh of the interior cells for each block, one can use an outer frame one cell deep (ghost cells) at the boundaries of the block. The interior cells adjacent to the ghost cells boundaries are termed first interior cells. The boundary conditions are handled in the discretized form through the flow properties of the ghost cells and the adjacent first interior cells.

2.3 Discretization of the flow equations

The required linear algebraic difference equations for the interior cells are obtained in two stages. The first stage is to integrate the general differential form of the flow equations over the individual control volume V_i of the i^{th} interior cell. Using the Gauss divergence theorem together with the assumption that the finite volume V_i is time invariant, the integration yields the discrete version of RANS equations expressed as:

$$V_i \frac{d}{dt} (\rho\phi)_i + \sum_{k=1}^{N_f} [(\rho\vec{U}\phi)_k \cdot \vec{n}_k S_k]_i = \sum_{k=1}^{N_f} [(\Gamma_\phi \nabla \phi)_k \cdot \vec{n}_k S_k]_i + V_i (S_\phi)_i \quad (4)$$

where N_f is the number of faces bounding the volume V_i , and \vec{n}_k and S_k are the outward unit normal vector and the surface area of the k^{th} face, respectively. The notation i included in the various terms of Equation (4) implies the average values over the volume V_i . The second stage is to obtain for $\phi \neq 1$ the linear algebraic difference equation in the unknown numerical value ϕ_p at the center of the i^{th} interior cell. This equation is derived from Equation (4) according to the following steps. The time derivative is expanded using first order (backward) differencing scheme. The space derivatives in the diffusion term are calculated using the central differencing scheme. The flux value in the convective term at each cell face is calculated by interpolation as the weighted mean of the corresponding values at the centers of the neighboring cells using the appropriate differencing scheme. The appropriate scheme is selected depending on the simplicity, accuracy, and computational time controlled by the flow field conditions. The present algorithm has the facility to utilize common differencing schemes known as, Hybrid, Power-Law, QUICK, and TVD [19]. The general mathematical dependence of the discrete source term in Equation (4) on the unknown variables ϕ_p is approximated by linear dependence in the form:

$$V_i (S_\phi)_i = S_u + S_c \phi_p \quad (5)$$

where the values of the constants S_u and S_c can be obtained from the linearization procedure of the given source function. Fulfilling the above-mentioned steps of the second stage, flowed by suitable mathematical rearrangement, the resulting linear algebraic equation in the unknown ϕ_p can be written as:

$$a_p \phi_p = a_p^o \phi_p^o + \sum (a_{nb} \phi_{nb}) + S_u \quad (6)$$

where ϕ_p^o is its value at the previous time, and ϕ_{nb} are the corresponding values at the centers of the neighboring cells.

2.4 Boundary conditions

To close the system of linear algebraic difference equations, Equation 6, the discrete form of the boundary conditions must be specified. The conditions imposed on the boundaries are defined using the ghost cells specified above in section 2.2. Two classes of boundary conditions must be specified. One class of fixed conditions to be imposed on the physical boundaries at the whole domain and another class of conditions is imposed at the interfaces between the blocks. The first class includes the common types of inflow, outflow, solid wall, far-field, and symmetry. The second class which is known as the connectivity boundary conditions describes the communication mechanism between neighboring blocks. The values describing the boundary conditions are functions of the flow variables for the first interior cell and the corresponding imposed variables on the ghost cell. These functions are specified depending on the class of the imposed conditions defined at the interface between the first interior cell and the ghost cell. For a physical boundary, the value of the ghost cell variable is extrapolated from the value of the interior cell variable and the fixed value of the boundary condition. On the other hand for the connectivity boundary, the value of the first interior cell variables adjacent to the connectivity interface are copied to the ghost cell of the neighboring block. The treatment of the wall boundary conditions with turbulent flows demands some special considerations particularly when the standard k- ϵ model of turbulence is used. Since such model becomes inadequate in near wall regions as described by Launder and Spalding [20]. Wall functions formulae in conjunction with the k- ϵ turbulence model [20] are used in the present study to bridge this region.

2.5 Numerical Solution methodology

The system of the linear algebraic equations, Equation 6, is solved using an iterative procedure. The robustness of the iterative solution is improved by introducing under-relaxation factor α_ϕ in order to slow down the change of dependent variables in consecutive solutions. Consequently Equation (6) becomes:

$$\frac{a_p}{\alpha_\phi} \phi_p = \sum (a_{nb} \phi_{nb}) + a_p^o \phi_p^o + \frac{(1 - \alpha_\phi)}{\alpha_\phi} a_p \phi_p^{n-1} + S_u \quad (7)$$

where the superscript ($n-1$) refers to the previous iteration. The strongly implicit procedure (SIP) [19] is used for the iterative solution of the linear algebraic equations, Equation (7). The present work adopts a pressure-based solution through the velocity-pressure coupling using the pressure correction approach in collocated grid arrangement. In this approach, the velocity fields obtained by solving Equation (7) are adjusted to satisfy the continuity equation. This task is achieved using semi-implicit SIMPLE algorithm together with Rie and Chow interpolation.

2.6 The in-house CFD code

An integrated in-house CFD code is developed in the present work for the implementation of the numerical solution. The code consists of three main elements: a pre-processor, a solver and a post-processor. The code elements are written in FORTRAN 90. The pre-processor receives all data and information required to specify the flow problem. Subsequently it logically and mathematically transforms the data and information into suitable form which are considered as the input of the flow solver. Accordingly, the pre-processor activities involve: defining the computational domain geometry, generating the grid of cells, selecting the transport phenomena that need to be modeled, and specifying the fluid properties as well as the appropriate boundary conditions. The flow solver fulfills the details and steps of the numerical solution stated in the previous section. The post-processor receives the output of the flow solver in the form of numerical predictions and presents it using versatile data visualization tools including: domain geometry and grid display, vector plots, and line and shaded contour plots. The input and output files of the flow solver are written according to CFD General Notation System (CGNS) standard [21]. Important tools visualizing the two-dimensional flow field are streamlines defined as contours of constant stream function ψ and associated contours for constant vorticity ω .

2.7 Verification and validation (V&V) process of the in house CFD code

The present in-house CFD code mathematically solves the flow equations associated with numerous physical phenomena, properties, geometries, and initial and boundary conditions. The discussion in the preceding sub-sections shows the two important features of this code. The first feature is that the code numerically simulates the interactions between the different physical items of the flow through a series of complex mathematical activities. Consequently, the code correctness and accuracy of its calculations must be verified. The second feature is that the physical items considered in the code are in general, complex in nature and are governed with known and well-established physical laws. Accordingly, the code ability to physically handle real flow situation must be validated. Thus, code verification and validation is required to complete the development of the present numerical algorithm. This process is performed in the next section by comparing the results computed by the present code for selected standard test cases, with available results computed from other well-established reference codes.

3. Results and discussions

This section is devoted for presenting and discussing the numerical results for four standard 2D test cases. The test cases have been chosen as representative for a broad range of CFD applications of weakly compressible flow for which the present CFD code can be applied. The verification of the code correctness is decided when the numerical results of the code, for all test cases, are in good qualitative and quantitative agreement with those from other well-established codes. The verification of the code calculations accuracy is decided through the relatively small deviation of the present numerical results from those of the other codes, averaged over the tested cases. On the other hand the validation of the code is decided by its ability to predict the physically complex flow features encountered in the different standard test cases.

3.1 The lid driven flow in a square cavity

The simple case of steady state lid driven laminar flow in a square cavity has been considered as the major test case. The case only uses the laminar Cartesian part of the code. Accordingly, the basic elements, the Rhie-chow interpolation, and boundary conditions can be tested without any disturbance from curvilinear part. Comparison results for this case are available through [22] and the NASA NPARC Alliance CFD Verification and Validation [23]. Figure 1 shows the main features of the lid-driven flow in a square cavity. In this case the fluid contained inside the cavity is set into motion by sliding a long plate (lid) with a constant velocity at the top of the cavity. The dimensionless Reynolds number Re and other dimensionless variables (x^*, y^*) and properties $(u^*, v^*, \psi^*, \omega^*)$ describing the generalized cavity flow are based on the plate velocity, U_{lid} , and the side length of the cavity, L . The figure shows that several standing vortices may exist whose occurrence is function of the Reynolds number Re . The big vortex shown and the other smaller ones are known as primary vortex and secondary vortices, respectively. The vortex patterns can be described by stream function contours known as streamlines whose characteristics of shape, dimensions and location are functions of Re . The contour with $\psi = 0$ shown in Figure 1 represents the border between the primary vortex and secondary ones. The triangles formed by this contour and its intersections with the cavity walls encompass the secondary vortices. Consequently, the triangular height H and the width W may be considered (for example) as characteristic dimensions of the secondary vortex at the bottom right corner of the cavity.

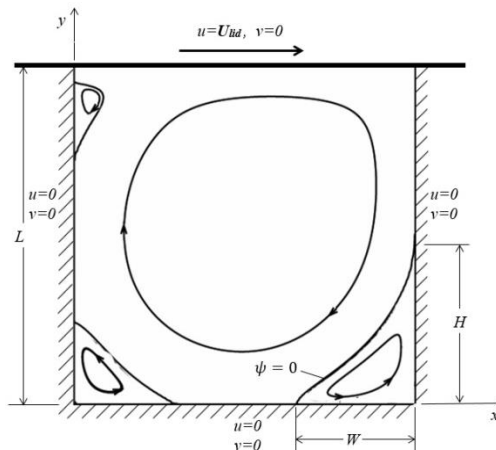


Fig. 1. The main features of the lid-driven flow in a square cavity with possible vortices.

Figure 2 shows the plots of streamlines, which are contours of the dimensionless stream functions ψ^* , for both the results of the present code and the results of Ghia et al. [22] benchmark solution. These streamlines describe the vortex patterns of the cavity flow with

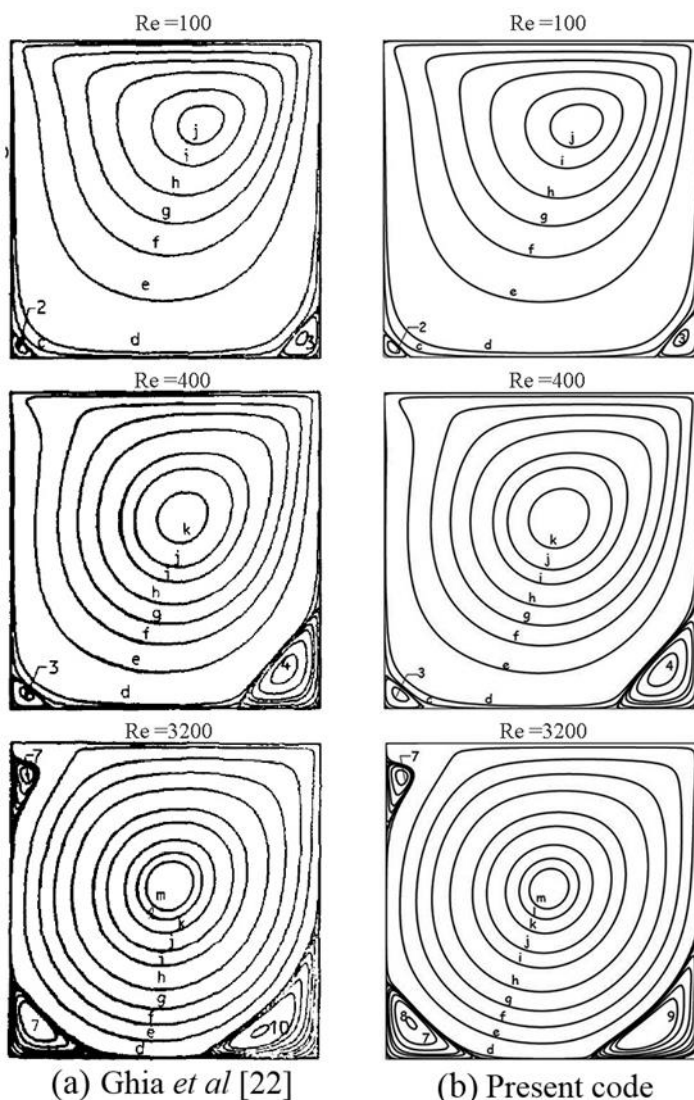


Fig. 2. Streamline pattern for primary and secondary vortices for the lid driven cavity flow.

Re representative values of 100, 400 and 3200. Figure 3 shows the contours of dimensionless vorticity ω^* for the same vortex patterns of the cavity flow described by the plots in Figure 2. The values of ψ^* and ω^* along the different contours in Figures 2 and 3 are listed in Table 2. The negative sign of ψ^* values for the contours of the streamlines describing the primary vortex indicates that the vortex rotates in a clockwise direction, in consistence with the direction of the lid plate velocity as shown in Figure 1. It can be seen from the plots in Figure 2, for all Re values that the results of the present code generally agree well with results of Ghia *et al.* [22]. This is evident by observing the same shape and dimensions of the streamlines describing the primary vortex despite the slight shift of its center location. Good agreement of the present code with [22] results is still retained regarding the occurrence and locations of the secondary vortices. This is understood by the existence of two secondary vortices at all Re values at the bottom corners while at $Re =$

3200 a third secondary vortex is formed at the upper left corner. Examining the plots in Figure 3 the characteristics of the vorticity contours emphasize the good quantitative and qualitative agreements between the results of the present code and the results of [22].

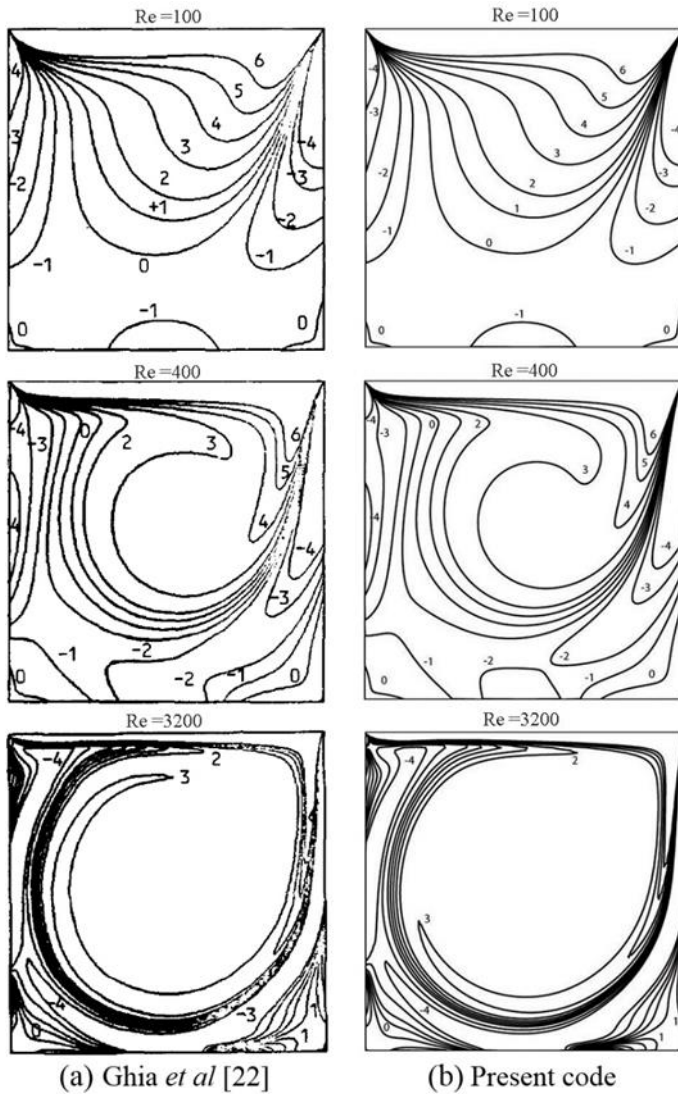


Fig. 3. Vorticity contours for the lid driven cavity flow.

Table 2.Values of ψ^* for Streamlines in Figure 2 and ω^* for Vorticity Contours in Figure 3

| Stream function, Figure 2 | | | | Vorticity, Figure 3 | |
|---------------------------|-------------------------|----------------|-----------------------|---------------------|---------------------|
| Contour letter | Value of ψ^* | Contour number | Value of ψ^* | Contour number | Value of ω^* |
| a | -1.00×10^{-10} | 0 | 1.00×10^{-8} | 0 | 0.0 |
| b | -1.00×10^{-07} | 1 | 1.00×10^{-7} | 1 | 0.5 |
| c | -1.00×10^{-05} | 2 | 1.00×10^{-6} | 2 | 1.0 |
| d | -1.00×10^{-04} | 3 | 1.00×10^{-5} | 3 | 2.0 |
| e | -0.0100 | 4 | 5.00×10^{-5} | 4 | 3.0 |
| f | -0.0300 | 5 | 1.00×10^{-4} | 5 | 4.0 |
| g | -0.0500 | 6 | 2.50×10^{-4} | 6 | 5.0 |
| h | -0.0700 | 7 | 5.00×10^{-4} | -1 | -0.5 |
| i | -0.0900 | 8 | 1.00×10^{-3} | -2 | -1.0 |
| j | -0.1000 | 9 | 1.50×10^{-3} | -3 | -2.0 |
| k | -0.1100 | 10 | 3.00×10^{-3} | -4 | -3.0 |
| l | -0.1150 | | | | |
| m | -0.1175 | | | | |

This can be emphasized by observing the same feature of high vorticity gradient indicated by the concentration of the vorticity contours as Re increases. A related comparative discussion can be made using a useful survey of numerical values of some important properties which are provided in Table 3. These properties are selected to characterize the primary vortex and a representative secondary one at the bottom right corner of the cavity. The values x^* , y^* and ω^* listed in this table correspond to the vortices centers at which $\psi^* = \psi^*_{min}$ (primary) or $\psi^* = \psi^*_{max}$ (secondary). Table 3 indicates that with the increase of Re number the center location of the primary vortex moves from the upper downstream corner toward the center of the cavity. This is consistent with the observations in Figure 2. For all properties the numerical values computed by the present code are almost of the same values as the results of [22], except small deviations.

Table 3.

Some important properties charactering the primary and secondary Vortices.

| Vortex | Property | Re=100 | | Re=400 | | Re=3200 | |
|-----------|----------------------|-------------------------|-----------------------|-------------------------|--------------------------|-------------------------|--------------------------|
| | | Present Code | Ghia et al. [22] | Present Code | Ghia et al. [22] | Present Code | Ghia et al. [22] |
| Primary | ψ^*_{min} | -0.103423 | -0.10422 | -0.113909 | -0.115081 | -0.120377 | -0.119435 |
| | $\omega^*_{v,c}$ | 3.16646 | 3.04429 | 2.29469 | 2.32737 | 1.98860 | 1.83992 |
| | Location, x^*, y^* | 0.6172, 0.7344 | 0.617, 0.7344 | 0.5547, 0.6055 | 0.5471, 0.6016 | 0.5165, 0.5469 | 0.5161, 0.5396 |
| Secondary | ψ^*_{max} | 1.2537×10^{-5} | 1.33×10^{-5} | 6.4235×10^{-5} | 6.78496×10^{-5} | 3.1396×10^{-5} | 2.88482×10^{-5} |
| | $\omega^*_{v,c}$ | -0.0330749 | -0.035179 | -0.433519 | -0.455139 | -2.27365 | -2.16324 |
| | Location x^*, y^* | 0.9453, 0.0625 | 0.9407, 0.0605 | 0.8906, 0.1250 | 0.8827, 0.1174 | 0.8125, 0.0859 | 0.8209, 0.0837 |
| | H^* | 0.1328 | 0.137451 | 0.2617 | 0.264167 | 0.3406 | 0.3526 |
| | W^* | 0.1484 | 0.154291 | 0.3203 | 0.33367 | 0.4102 | 0.4113 |

A more useful quantitative discussion for the comparison with [22] results can also be made using the velocity profiles u^* and v^* in the horizontal and vertical directions at the middle sections as shown in Figures 4 and 5 respectively. The behavior of the velocity profiles at different Re numbers is also an evidence of the good qualitative and quantitative agreement with the results [22]. Thus, it can be stated that to a large extent the present code correctness is verified.

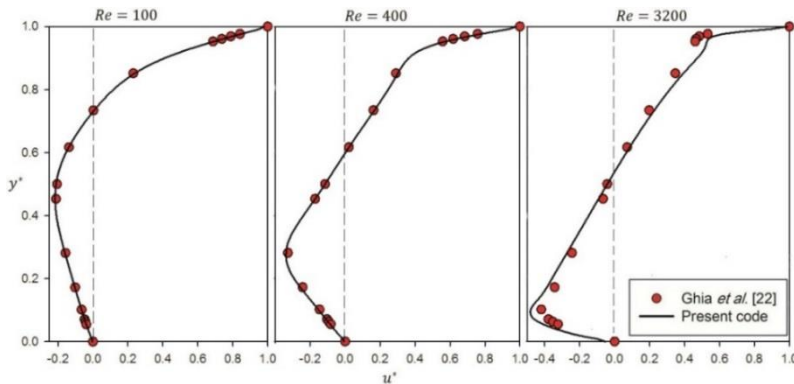


Fig. 4. The flow velocity profile in the x-direction along vertical plane passing through the geometric center of the cavity ($x^* = 0.5$).

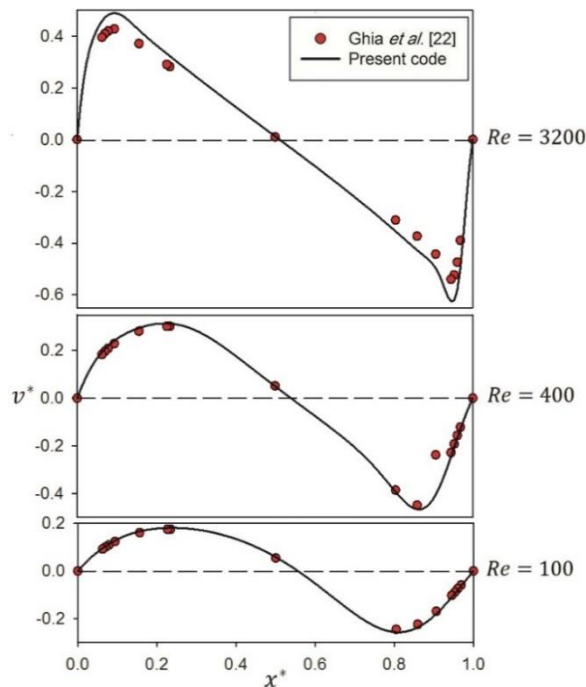


Fig. 5. The flow velocity profile in the y-direction along horizontal plane passing through the geometric center of the cavity ($y^* = 0.5$)

One more check has been carried out in which the results of the velocity distribution computed by the present code are plotted and compared with those of the WIND CFD code as given in [23]. This is presented in Figure 6 by contours of Mach number. Comparison

indicates the good agreement between the results of the present code and the results of the WIND CFD code especially at low values of Re number. This agreement is another indication for the verification of the present code correctness for this test case.

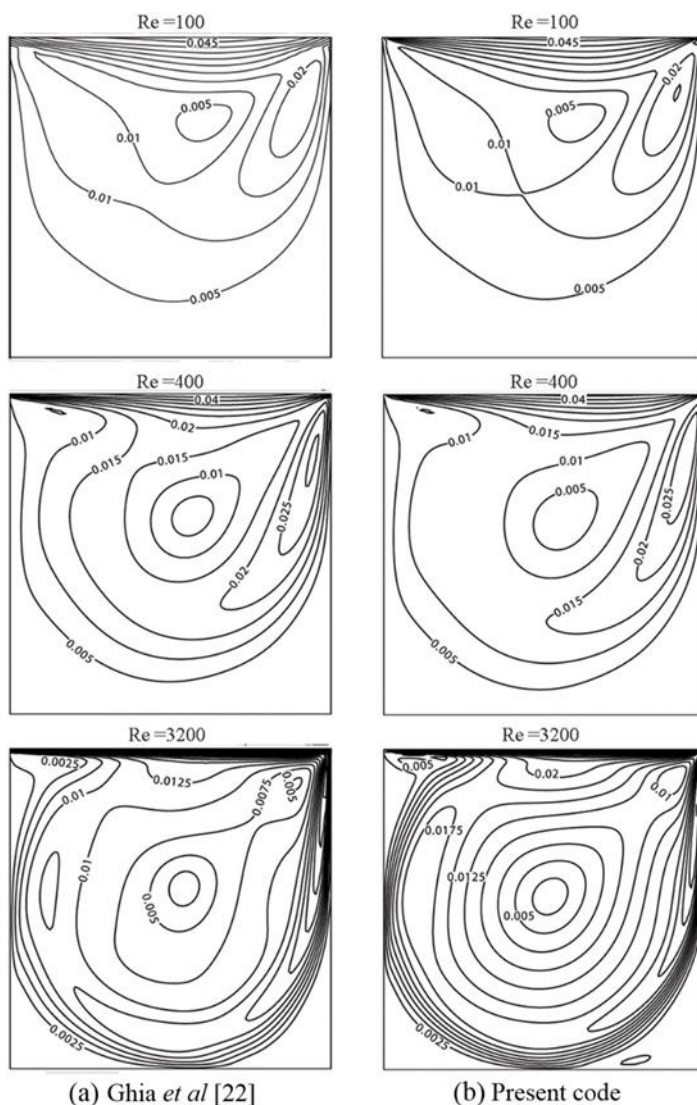


Fig. 6. Contours of Mach number for the lid driven flow in a square cavity.

In the absence of the exact solution, an indicator can be introduced for the accuracy of the calculations of the present code by comparing its results with the available calculations of more accurate well-established codes. Therefore, the results in Table 3 together with those of the velocity profiles presented in Figures 4 and 5 were considered to estimate the average relative deviation of the present code calculations from those obtained by [22]. The estimation procedure produced an average relative deviation of +1.47% for the numerical values in Table 3, and an average of +5.7% for the numerical values of the velocity profiles in Figures 4 and 5. A weighted mean of +4.29% of the relative deviation was obtained as a representative for all numerical values discussed for the test case. This

acceptable value of the relative deviation is small enough to consider that the present code calculations accuracy is verified.

3.2 The flow over a bump in a channel

The flow over a bump in a channel is another useful test case that has been selected to test the general turbulent curvilinear part of the present code. Therefore, the code curvilinear coordinates are manipulated to deal with the curvature of the bump wall. On the other hand, the flow is kept turbulent using appropriate uniform conditions ($\rho_\infty, u_\infty, P_\infty, T_\infty$) of the parallel inflow combined with the bump profile shape and characteristic base length L . Moreover, this case introduces noticeable non-zero pressure gradients on the bump wall. Comparison results of this case are those computed using the CFL3D reference code available through the NASA Langley Research Center [24]. Figure 7 shows the overall computational domain and boundary conditions together with a close-up of the flow region near the bump. The bump is an adiabatic solid wall, which extends in the direction of the dimensionless ordinate $x^* = x/L$, between $x^* = 0.0$ and $x^* = 1.5$. The flat part of the bump wall is described by $y_0^* = 0.0$. The curved part of the bump wall between $x^* = 0.3$ and $x^* = 1.2$ has a profile $y_0^* = y/L$ defined by the relation shown in Figure 7b. Both the present and reference codes were run at a Mach number $M = 0.2$ and Reynolds number $Re_L = 3E6$ based on the inflow velocity u_∞ and the characteristic length L . Due to the limitation on the CPU time, a grid of 352 (in the stream-wise direction) x 160 (in the normal direction) cells is used in the present code to discretized the overall domain, Figure 7a, while the corresponding results used for comparison are those computed by the reference code using a fine grid (1408 x 640 cells).

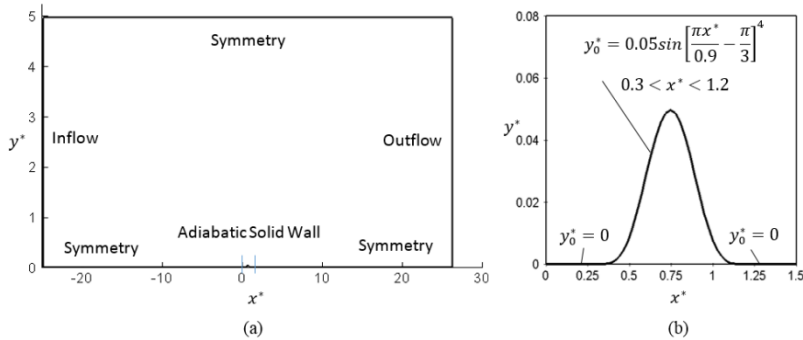


Fig. 7. Space domain of the flow over a bump in a channel: (a) overall computational domain and boundary conditions, and (b) close-up of the flow region near the bump.

The results for the flow region shown in Figure 7b are presented in the following plots: a plot of surface pressure coefficient $C_p = (P - P_\infty)/(0.5\rho_\infty u_\infty^2)$ in Figure 8, a plot of velocity profiles $u^* = u/u_\infty$ at the locations of $x^* = 0.0$ and $x^* = 1.2048$ in Figure 9, and a plot of contours of turbulence kinetic energy $k^* = k/U_{sound}^2$ in Figure 10. The variation of these parameters illustrates the complex flow features near the bump wall. The results of the present code in Figures 8-10 almost show good qualitative and quantitative agreement with the reference code results except for the small deviations associated with the less fine mesh used in the present code.

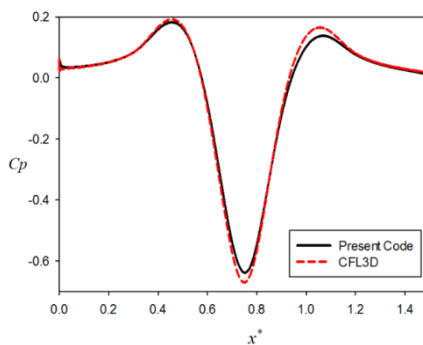


Fig. 8. Surface Pressure coefficient at the bump wall ($y^* = y_0^*$)

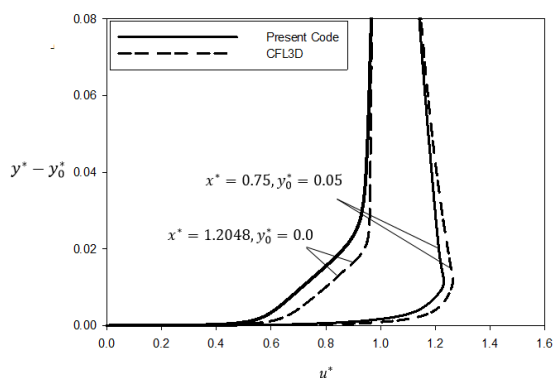


Fig. 9. Velocity profiles at $x^* = 0.75$ and $x^* = 1.2$

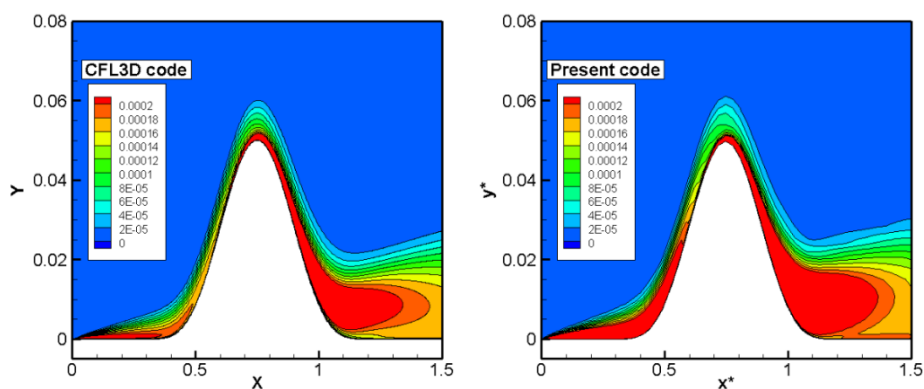


Fig. 10. The turbulent kinetic energy, k^* , contours

3.3 Downstream-facing step with time varying inflow

The third test case deals with the flow past a downstream-facing step generated by harmonic variation in time of the inflow velocity. This case is an example of unsteady viscous confined flows. The case has been chosen to demonstrate the use of unsteady RANS equations and to test the multi-block facility of the present code. The results of the present code for this test case are compared with those of computational solutions as given by Mateescu et al. [25] using an efficient time-accurate numerical method. Figure 11 shows the computational domain consisting of two blocks together with the dimensions

and boundary conditions. The downstream channel length of $15H$ is expected to be large enough to apply the outflow condition at the exit of the channel. The flow is referred to the Cartesian coordinates x and y centered at the step corner. The Reynolds number Re and the other dimensionless variables of the flow are based on the downstream channel height H , and the mean inflow velocity U_0 . An oscillating fully developed laminar flow describing the inflow condition is defined (in dimensionless form) by:

$$u^*(y^*, t^*) = \frac{U(y, t)}{U_0} = 24(1 - A \sin \Omega^* t^*) y^*(0.5 - y^*) \quad (8)$$

where $t^* = t U_0 / H$, $\Omega^* = \Omega H / U_0$ and A are the dimensionless values of time, angular frequency, and amplitude of the inflow velocity oscillation, respectively.

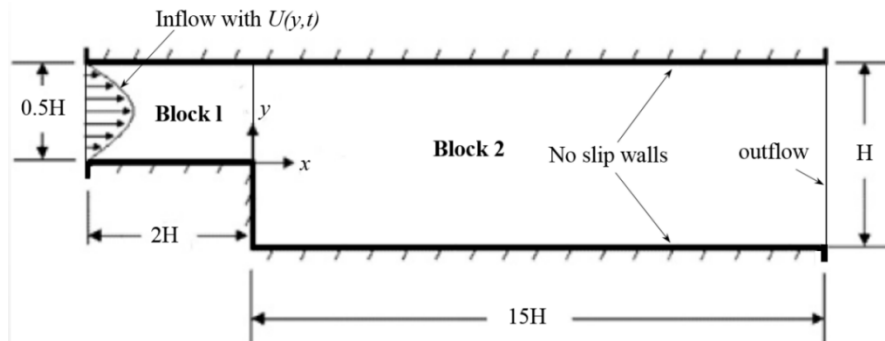


Fig. 11. The computational domain of the flow past a downstream-facing step.

Figure 12 shows the results for streamline patterns for the unsteady flow at various moments during the oscillatory cycle, t^*/τ^* (where $\tau^* = 2\pi/\Omega^*$ is the dimensionless period of the inflow velocity oscillations). These results were computed with $Re = 600$, $\Omega^* = 0.05$, and $A = 0.4$. These flow features illustrate the parallel flow behavior in most of the upstream channel and near the downstream channel exit. In addition, the lower wall primary separation region downstream the step is always present during the whole oscillatory cycle. On the other hand the upper wall separation region and the lower wall secondary separation region disappear at certain moments of this cycle as shown at $t^*/\tau^* = 0.4$ in Figure 12. The results of the present code are in good qualitative and quantitative agreement with those of [25]. The agreement can be noticed from the nearly same trend and shape of the streamlines as well as the shape, dimensions and locations of the separation regions. This agreement is an indication of the present code verification for the investigated test case.

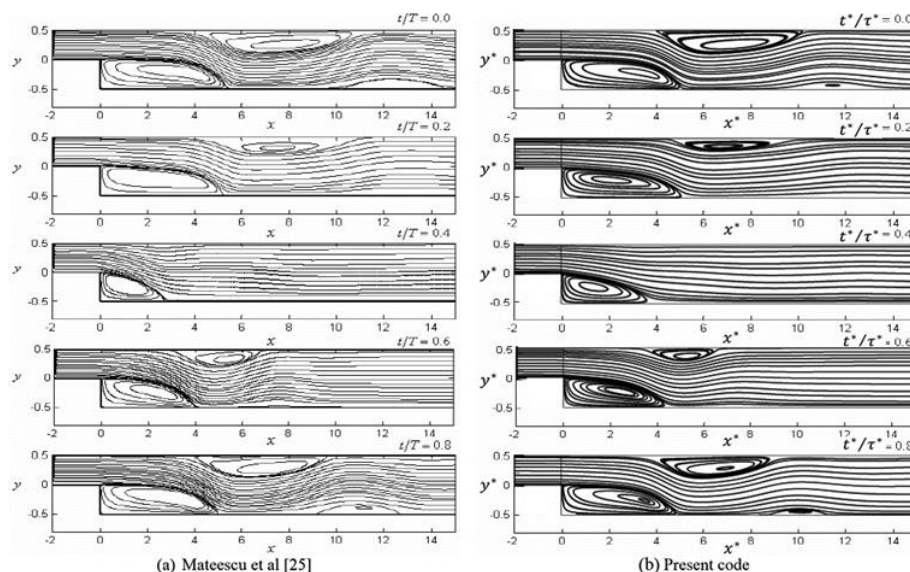


Fig. 12. Streamline patterns for the unsteady flow past a downstream-facing step. [Parameters x , y , t and T shown in (a) are dimensionless]

3.4 Forced-convection flow over flat plate

The application of the present code to heat transfer flow problems is checked by considering the simple case of parallel flow over a hot flat plate. This test case is selected to demonstrate the use of the energy equation in the present code. Available comparison results for this case obtained by reference solutions as presented in Schlichting [26]. Figure 13 shows the overall computational domain with the dimensions and boundary conditions for the steady parallel flow over a flat plate at zero incidence. The figure shows the thickness profile $\delta(x)$ of the growing boundary layer. This profile divides the fluid flow into two distinct regions: fluid film (the boundary layer) and the free stream. The test case was run with constant fluid properties estimated at a fluid film temperature $T_f = (T_\infty + T_w)/2$. Appropriate flow conditions (u_∞, T_∞, T_w and L) were chosen to insure dominant forced convection with laminar ($Re_L = 43000$) incompressible ($M = 0.008$) flow through the whole domain. The estimated maximum boundary layer thickness δ for these conditions is about $0.02L$, so the indicated domain height is large enough to consider outflow condition at the upper boundary.

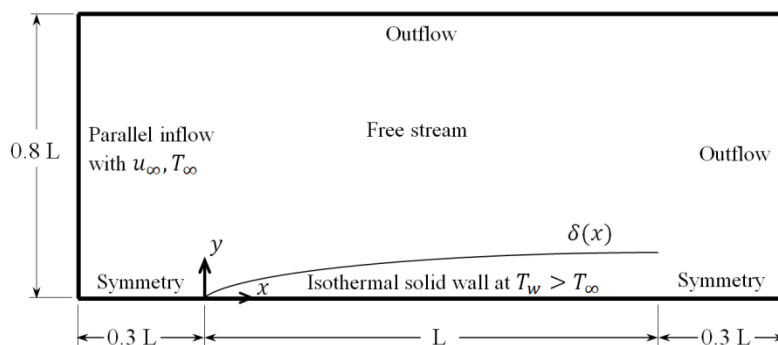


Fig. 13. Computational domain for forced convection flow over a flat plate.

The forced convection flow over the flat plat can be characterized by some useful dimensionless flow properties which are functions of the local Reynolds number Re_x . These are the velocity component $u^* = u/u_\infty$, the normalized velocity boundary layer thicknesses δ/x , and the dimensionless heat transfer coefficient (known as Nusselt number) $Nu_x = -x \frac{\partial T}{\partial y} \Big|_{y=0} / (T_w - T_\infty)$. The corresponding results are shown in Figure 14 for the velocity profile u^* vs. $\eta = y\sqrt{u_\infty/\nu x}$, and in Table 4 for the other flow and heat transfer characteristics. The present code is mostly in good agreement with the reference solutions. Similar to the first test case, an average relative deviation of the present code calculations from those by the reference solutions is used to account for the code calculations accuracy. An average relative deviation of (5.5%) was estimated based on the results shown in Figure 14 and Table 4. This small value is another indication of the accuracy of the present code calculations.

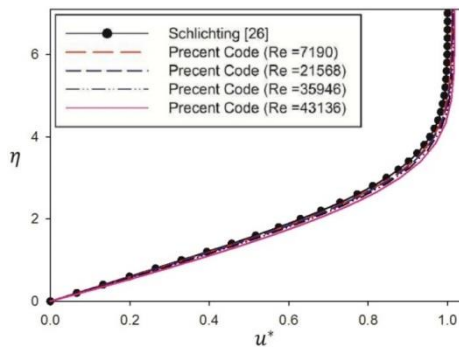


Fig. 14. The velocity profiles for laminar flow of forced convection over a flat plate.

Table 4.

Flow and heat transfer characteristics of forced convection over a flat plate.

| | | Present code | | Schlichting 1979 | |
|------|--------|--------------|--------|------------------|--------|
| x | Re_x | δ/x | Nu_x | δ/x | Nu_x |
| 0.01 | 1434 | 0.1230 | 11.19 | 0.1320 | 11.39 |
| 0.05 | 7169 | 0.0538 | 25.01 | 0.0591 | 25.23 |
| 0.10 | 14337 | 0.0376 | 35.36 | 0.0418 | 35.79 |
| 0.15 | 21506 | 0.0308 | 43.33 | 0.0341 | 43.88 |
| 0.20 | 28674 | 0.0263 | 50.03 | 0.0295 | 50.82 |
| 0.25 | 35843 | 0.0232 | 55.93 | 0.0264 | 57.41 |
| 0.29 | 41578 | 0.0208 | 60.24 | 0.0245 | 63.52 |

Finally, the above discussion of all considered test cases shows that an overall good agreement is obtained for the present code results with those of reference codes and solutions. This agreement together with the acceptable code accuracy and its ability to precisely predict the various complex flow features and conditions encountered in all test cases support the decision of the code verification and validation.

4. Conclusions

This paper presents the development of an accurate and efficient semi-implicit pressure-based algorithm with in-house CFD code to solve Navier-Stokes equations and energy equation governing weakly compressible single-fluid flow. A finite-volume discretization technique is introduced to produce structured non-orthogonal multi-block boundary-fitted curvilinear meshes with co-located grid arrangement. The algorithm uses high order schemes to approximate advective, diffusive, and non-linear terms of the flow equations. A satisfactory verification and validation (V&V) process for the CFD code of the present developed algorithm has been performed by comparing its results with the results of well-established reference CFD codes and solutions. The V&V process uses four standard test cases covering a broad range for CFD applications of weakly compressible flow. The present code results for all test cases are in good agreement with those of the reference codes and solutions. This agreement together with the code acceptable accuracy establishes the present code verification and validation.

5. Nomenclature

Latin Symbols

| | |
|-----------------|--|
| C_p | Pressure coefficient |
| c_p | Specific heat of the flow, $J \cdot kg^{-1} \cdot K^{-1}$ |
| F_x, F_y, F_z | Cartesian components for total external body forces per unit volume of the gas in x, y, and z directions, respectively, $N \cdot m^{-3}$ |
| H | The downstream channel length, m |
| h | Specific enthalpy energy of the gas, $J \cdot kg^{-1}$ |
| k | Turbulent kinetic energy, $m^2 \cdot s^{-2}$ |
| L | Side length of the cavity and Flat plate length, m |
| p | Pressure of the gas, Pa |
| \dot{Q} | Thermal energy generation rate per unit volume, W/m^3 |
| Re | Reynolds number. |
| S_ϕ | Source function associated with a generic form of the transport fluid property ϕ |
| S_k | Surface area of the k^{th} face of the interior cell |
| T | Fluid flow temperature, K |
| T_f | Fluid film temperature, K |
| T_{ref} | Reference temperature, K |
| T_w | Wall temperature, K |
| T_∞ | Inflow temperature, K |
| t | Time, s |
| \vec{U} | Flow velocity vector, $m \cdot s^{-1}$ |
| U_{lid} | Sliding lid plate velocity, $m \cdot s^{-1}$ |

| | |
|--------------------|---|
| U_o | Mean velocity of the inflow, m.s^{-1} |
| U_{sound} | Sound speed corresponding to the flow condition, m.s^{-1} |
| u_∞ | Inflow velocity, m.s^{-1} |
| u, v, w | Cartesian components of the flow velocity vector, m.s^{-1} |
| V_i | Volume of the i^{th} interior cell, m^3 |
| x, y, z | Cartesian coordinates |

Greek Symbols

| | |
|----------------------|---|
| α_ϕ | Relaxation factor |
| δ | Hydrodynamic boundary layer thickness, m |
| δ_t | Thermal boundary layer thickness, m |
| ε | Dissipation rate of the turbulent kinetic energy, $\text{m}^2.\text{s}^{-3}$ |
| ψ | Stream function, $\text{m}^2.\text{s}$ |
| Γ_ϕ | Effective exchange (diffusion) coefficient associated with a generic form of the transport fluid property ϕ |
| μ | Dynamic molecular viscosity of the gas phase, $\text{kg.s}^{-1}.\text{m}^{-1}$ |
| μ_e | Effective dynamic viscosity included in the viscous terms of the source function for gas-phase momentum balance, $\text{kg.s}^{-1}.\text{m}^{-1}$ |
| μ_t | Turbulent viscosity of the gas phase, $\text{kg.s}^{-1}.\text{m}^{-1}$ |
| Ω | Angular frequency of oscillation, rad.s^{-1} |
| ω | Vorticity, s^{-1} |
| ϕ | Generic form of the transport fluid property |
| ρ | Fluid flow density, kg.m^{-3} |
| ρ_∞ | Inflow density, kg.m^{-3} |
| σ_h | Turbulent Prandtl number for enthalpy energy |
| σ_k | Turbulent Prandtl number for kinetic energy of turbulence |
| σ_ε | Turbulent Prandtl number for dissipation rate of turbulent energy |
| τ | Time period of oscillation, s^{-1} |

REFERENCES

- [1] Hasib, R., Kumar, R., Shashi, and Kumar, S. Simulation of an Experimental Compartment Fire by CFD. *Building and Environment* 2007; 42: 3149–3160.
- [2] Jia, F., Galea, E.R., and Patel, M.K. The Numerical Simulation of the Noncharring Pyrolysis Process and Fire Development within a Compartment. *Applied Mathematical Modelling* 1999; 23: 587-607.
- [3] Merci, B., and Maele, K.V. Numerical Simulations of Full-Scale Enclosure Fires in a Small Compartment with Natural Roof Ventilation. *Fire Safety Journal* 2008; 43: 495–511.
- [4] Suard, S., Lapuerta, C., Babik, F., and Rigollet, L. Verification and Validation of a CFD Model for Simulations of Large-Scale Compartment Fires. *Nuclear Engineering and Design* 2011; 241: 3645-3657.
- [5] Cai, N., and Chow, W.K. Air Flow through the Door Opening Induced by a Room Fire under Different Ventilation Factors. *Procedia Engineering* 2012; 43: 125–131.
- [6] Hu, L.H., Peng, W., and Huo, R. Critical Wind Velocity for Arresting Upwind Gas and Smoke Dispersion Induced by Near Wall Fire in a Road Tunnel. *Journal of Hazardous Materials* 2008; 150: 68-75.
- [7] Rigas, F., and Sklavounos, S. Simulation of Coyote Series Trials–Part II: A Computational Approach to Ignition and Combustion of Flammable Vapor Clouds. *Chemical Engineering Science* 2006; 61: 1444–1452.

- [8] Grishin, A.M. *Mathematical Modeling of Forest Fires and New Methods for Fighting Them*. Tomsk, Russia: Publishing House of the Tomsk University, 1997.
- [9] Larini, M., Giroud, F., Porterie, B., and Loraud, J.C. A Multiphase Formulation for Fire Propagation in Heterogeneous Combustible Media. *Int. J. Heat Mass Transfer* 1998; 41: 881-97.
- [10] Morvan, D., and Dupuy J.L. Modeling of Fire Spread through a Forest Fuel Bed Using a Multiphase Formulation. *Combust. Flame* 2001; 127: 1981-94.
- [11] Morvan, D., and Dupuy J.L. Modeling the Propagation of a Wildfire through a Mediterranean Shrub Using a Multiphase Formulation. *Combust. Flame* 2004; 138: 199-210.
- [12] Perry, G.L.W. Current Approaches to Modeling the Spread of Wildland Fire: a Review. *Prog. Phys. Geogr.* 1998 , 22(2): 222-45.
- [13] Porterie, B., Consalvi, J.L., Loraud, J.C., Giroud, F., and Picard, C. Dynamics of Wildland Fires and their Impact on Structures. *Combust. Flame* 2007; 149: 314-28.
- [14] Sardoy, N., Consalvi, J.L., Porterie, B., and Fernandez-Pello, A.C. Modeling Transport and Combustion of Firebrands from Burning Trees. *Combust. Flame* 2007, 150: 151-69.
- [15] El-Zohri, E.H., Shafey, H.M., Abdel-Salam, M., and Ahmed, A. Mathematical modeling of agricultural fires beneath high voltage transmission lines. *Energy* 2011; 36: 385-396.
- [16] El-Zohri, E.H., Abdel-Salam, M., Shafey, H.M., and Ahmed, A. Mathematical Modeling of Flashover Mechanism due to Deposition of Fire-Produced Soot Particles on Suspension Insulators of a HVTL. *Electric Power Systems Research* 2013; 95: 232–246.
- [17] Novozhilov, V. Computational Fluid Dynamics Modelling of Compartment Fires. *Progress in Energy and Combustion Science* 2001 27(6): 611-666.
- [18] Sørensen, N.N. *General Purpose Flow Solver Applied to Flow over Hills*. Risø-R- 827-(EN), Risø National Laboratory, Roskilde, Denmark, 2003.
- [19] Ferziger, J. H. and Peric, M. *Computational Methods for Fluid Dynamics*. 2nd ed., Springer-Verlag, 2011.
- [20] Launder, B. E. and Spalding, D.B. *The Numerical Computation of Turbulent Flows*. *Computer Methods in Applied Mechanics and Engineering* 1974; 3(2): 269-289.
- [21] Rumsey, C., Allmaras, S., Alonso, J., Bush, B., et al. *The CFD General Notation System Standard Interface Data Structures*. AIAA Recommended Practice, No. R101A-2005, Published by the American Institute of Aeronautics and Astronautics, Reston, VA, USA. 2005.
- [22] Ghia, U., Ghia, K. N., and Shin, C. T. High-Re Solutions for Incompressible Flow Using the Navier-Stokes Equations and a Multigrid Method. *Journal of Computational Physics* 1982; 48: 387-411.
- [23] Slater J. W. and et al. Driven Cavity. <http://www.grc.nasa.gov/WWW/wind/valid/cavity/cavity.html>.
- [24] Rumsey, C. et al. 2D Bump-in-Channel Verification Case - Intro Page. <http://turbmodels.larc.nasa.gov/bump.html>.
- [25] Mateescu, D., Mei, C.B., and Zuppel, E. Computational Solutions of Unsteady Confined Viscous Flows with Variable Inflow Velocities for Unsteady Fluid-Structure Interaction Problems. *Proceedings of the Symposium of Flow-Induced Vibrations-2005, ASME PVP Conference, Denver, Colorado, July 2005, ASME Paper PVP2005-71777: 1-11.*
- [26] Schlichting, H. *Boundary Layer Theory*. McGraw-Hill, New York, 1979.

استنباط واختبار صحة ودقة وتحقيق كود خاص لديناميكا الموائع الحسابية لنمذجة سريان انضغاطي ضعيف

الملخص العربي

تقدم هذه الورقة بحثاً يمثل المرحلة الأولى من برنامج شامل للنمذجة والحل الحسابي العددي يستخدم في بحث يجري الإعداد له في مجال الحرائق الزراعية وذلك في مختبر البحوث البيئية بجامعة اسيوط. تقدم الورقة طريقة (خوارزمية) دقيقة وفعالة يستنبط فيها معادلات ومتوسط قيم خواص السريان وحلها على اساس الضغط وبشكل شبه ضمني، وهذه المعادلات توصف وتحكم سريان انضغاطي ضعيف. يستخدم الحل العددي في الخوارزمية المعروضة تقنية الحجم المحدود مطبقة على شبكات ذات بناء عام ومتعددة النطاقات مكونة من خلايا ذات اضلاع منحنية غير متعامدة وهذه الخلايا مرتبة بالتجاور. وتشمل اللوغاريتم كود ديناميكا موائع حسابية متكامل استنبط خصيصاً لتنفيذ برنامج الحل العددي ويتكون الكود من ثلاثة مجموعات وهي خطوات الإعداد المسبق للمدخلات وبرنامج الحل وخطوات اعداد وعرض المخرجات. ويخضع الكود لعملية قياسية لاختبار صحة علاقاته ودقة حساباته والتحقق من مدى استخدامه في التطبيقات المختلفة وتستخدم في هذه العملية مجموعة قياسية من حالات تمثل تطبيقات متنوعة لسريان الموائع. وقد وجد من استعراض ومناقشة النتائج العددية لهذه الحالات ان الكود المستنبط في البحث الحالي يتطابق بشكل كبير مع الاكواد القياسية المرجعية. وهذا يؤكد على صحة الكود ودقة حساباته وامكانية استخدامه في تطبيقات مختلفة.